Vortex patterns in a mesoscopic superconducting rod with a magnetic dot

Mauro M. Doria,[1,*] Antonio R. de C. Romaguera,[2] and F. M. Peeters[3,4]
[1]*Departamento de Física dos Sólidos, Universidade Federal do Rio de Janeiro, 21941-972 Rio de Janeiro, RJ, Brazil*
[2]*Departamento de Física, Universidade Federal Rural de Pernambuco, 52171-900 Recife, PE, Brazil*
[3]*Departement Fysica, Universiteit Antwerpen, Groenenborgerlaan 171, B-2020 Antwerpen, Belgium*
[4]*Departamento de Física, Universidade Federal do Ceará, 60455-760 Fortaleza, CE, Brazil*
(Received 14 July 2009; published 31 March 2010)

We study a mesoscopic superconducting rod with a magnetic dot on its top having its moment oriented along the axis of symmetry. We study the dependence of the vortex pattern with the height and find that for very short and very long rods, the vortex pattern acquires a simple structure, consisting of giant and of multivortex states, respectively. In the long limit, the most stable configuration consists of two vortices, that reach the lateral surface of the rod diametrically opposed. The long rod shows reentrant behavior within some range of its radius and of the dot's magnetic moment. Our results are obtained within the Ginzburg-Landau approach in the limit of no magnetic shielding.

DOI: 10.1103/PhysRevB.81.104529 PACS number(s): 74.78.Na, 74.25.−q, 74.20.De

I. INTRODUCTION

Magnetism and superconductivity are competing orders and its coexistence has been intensively investigated both in nanofabricated materials[1,2] and also in natural compounds.[3–8] Together they bring new phenomena such as in case of magnetic dots on top of a superconducting film which become a ratchet potential for moving vortices.[9,10]

The vortex pattern of a single mesoscopic disk can be determined in the extreme limits of a constant homogeneous magnetic field and of an inhomogeneous one, produced by a magnetic dot on its top. This has been investigated both theoretically[11–14] and experimentally,[2,15–18] however only in the limit of thin disks and films. In this paper, we study the thick disk, i.e., a "rod" with cylindrical shape (radius R and height z_0), as shown in Fig. 1. The height can be much larger than the coherence length, ξ. Thus the rod can be longer than a disk (height comparable to ξ) and shorter than a wire (micron-size height).

In this paper, we find the vortex pattern of a superconducting mesoscopic rod caused by the presence of a magnetic dot on its top, taken to be a point like magnetic moment μ aligned to the central axis. The magnetic field falls with the cubic power of the distance and, consequently, is weaker at the bottom surface of the rod as compared to the top one, leading to vortex patterns very distinct from the thin limit cases. The vortices become truly three-dimensional curved lines in space instead of the flat "coin" vortices found in the previous two-dimensional studies. Thus the height of the rod is a key parameter that renders the extreme cases of very short and very long rods different. The field spatial decay is not relevant for the short rod, and so, vortices pierce the rod top to bottom. The field intensity is concentrated at the rod's axis of symmetry, making possible the nucleation of giant vortices there. However, for the long rod, the cubic fall and the curvature of the magnetic field streamlines favor the onset of curved vortices running from the top to the side surface of the rod instead of reaching its bottom. Notice that for a very long rod even an intense magnetic moment cannot destroy the superconducting state, which always survive near the bottom. We find here that intermediate heights comprise very elaborate vortex patterns that mix features of both extreme limits. We show here that a long rod with small radius ($R \sim 2\xi$) has a reentrant behavior,[19] hence of interest for technological applications. This means that the entrance and the exit of a vortex is achieved by increasing the magnetic field generated by the dot. Thus the present system qualifies for technological applications as a logic gate to perform logical operation in digital circuits.[20] We study rods with radii $R=2\xi$, 3ξ, and 4ξ and in each case, we take selected heights, ranging from $z_0=2\xi$ to $z_0=5R$. Our results are obtained in the context of the Ginzburg-Landau (GL) theory in the limit of no magnetic shielding.

The mesoscopic superconductor gained notoriety when the magnetic properties of very thin superconducting mesoscopic disks were experimentally measured[21–23] for several radii and found to be in agreement with theoretical studies[24,25] based on the Ginzburg-Landau theory. The mesoscopic superconductor is intrinsically metastable and presents hysteresis even without the presence of pinning centers. This is because of energetic barriers separating different vortex states. The rod with a magnetic moment on top also shows these features. Recent experiments revealed a shell structure for the vortex patterns of the mesoscopic superconductor which are accurately described by theory.[26] Giant vortices are observed in Bose-Einstein condensates,[27] similarly to mesoscopic superconductors, where they have been recently detected.[26,28] Mesoscopic superconductors and Bose-Einstein condensates are useful systems to understand many aspects of vortex physics, such as curved vortices due to geometrical surface constraints[29,30] and the coexistence of vortices with different lengths[31] caused by asymmetry in the geometry. Top to bottom and top to side vortices are also found when the rod is in the presence of an homogenous magnetic field tilted with respect to the central axis.[31] Top to side vortices can exist for a magnetic field oriented with the main axis in case of a cone,[32] a geometry useful to understand the physics of scanning tunneling microscopy done with a superconducting tip. Recently we have shown that a magnetic moment inside the superconductor yields a vortex pattern that consists of fully developed three-dimensional

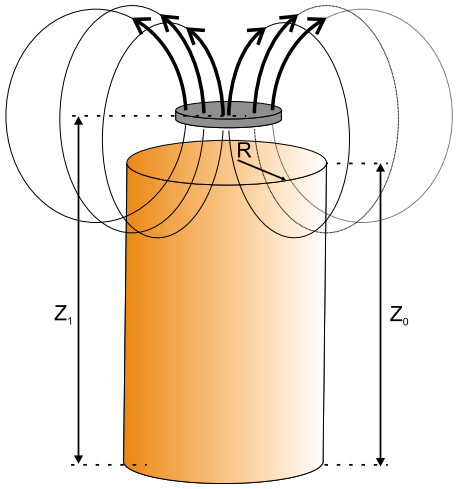

FIG. 1. (Color online) This figure depicts the magnetic dot on top of the superconducting rod and its dipolar field able to produce curved vortices inside the superconductor.

vortex loops.[33] Here we show that inside the rod vortices are also three-dimensional lines, though not as fully developed loops since the magnetic moment is outside the superconductor.

This paper is organized as follows. In Sec. II, we discuss the order parameter within the two harmonic component approximation. The next Sec. III is dedicated to the treatment of the Ginzburg-Landau theory with this two-component approximation. In Sec. IV, we analyze our numerical results describing the vortex patterns for the superconducting rod with a magnetic dot on top, and, finally in Sec. V, we conclude and summarize our results.

II. TWO-COMPONENT ORDER PARAMETER

The two-component approach is the simplest of all methods able to solve the full nonlinear GL theory. Besides the ground state, the excited states can also be determined by this method. It also provides a way to follow the evolution of a vortex pattern with well-defined angular momenta according to some external parameter, here being the magnetic moment μ. We apply it to describe a giant-vortex (GV) state, that pierces the rod top to bottom and the multivortex (MV) state, which contains the curve vortex lines that pierce the rod top to side.

We introduce cylindrical coordinates (ρ,φ,z) whose origin (0,0,0) is at the intersection of the axis of symmetry with the bottom of the rod. The system has azimuthal symmetry and in these coordinates, the order parameter has components of the form $\psi(\rho,\varphi,z)=\psi_L(\rho,z)\exp(iL\varphi)$, where the angular momentum quantum number L is an integer due to the single valuedness of the order parameter. The GV state contains just one angular momentum L,

$$\Psi(\rho,\varphi,z) = C_L\psi_L(\rho,z)e^{iL\varphi} \tag{1}$$

whereas the MV state has two angular momenta,

$$\Psi(\rho,\varphi,z) = C_{L_1}\psi_{L_1}(\rho,z)e^{iL_1\varphi} + C_{L_2}\psi_{L_2}(\rho,z)e^{iL_2\varphi}. \tag{2}$$

If one of the coefficients (C_{L_1}, C_{L_2}) vanishes the GV state is retrieved from the MV state.

This two-component order parameter is able to describe the nontrivial changes that take place in the vortex pattern, as the vortices change in shape, from a simple flat "coins" to a three-dimensional line shape by increasing the height. First, recall that at the center of a vortex the order parameter must vanish, $\Psi=0$. Therefore, we search for points of vanishing order parameter to detect the centers of GV and MV states described by Eqs. (1) and (2), respectively. For the GV state, the center of the vortex falls in the axis of symmetry, $\psi_L(\rho=0,z)=0$. For the MV state, the vortex centers are given by

$$e^{i(L_2-L_1)\varphi} = -\frac{C_{L_1}\psi_{L_1}(\rho_v,z_v)}{C_{L_2}\psi_{L_2}(\rho_v,z_v)}. \tag{3}$$

In case the right-hand side is equal to one, the equation becomes $\exp(iL\varphi)=1$, $L\equiv L_2-L_1$. Numerical analysis shows that this is possible only once for a radius ρ_v and height z_v, and a coefficient ratio C_{L_1}/C_{L_2}. Thus for each intersecting z plane, there are L solutions, $\varphi=0,2\pi/L,\ldots,(L-1)2\pi/L$, which correspond to the centers of equally spaced vortices set on a ring. The description of curved vortex lines, say, top to side vortices, through Eq. (3) means that there must exist solutions for an increasing ring (radius ρ_v) and decreasing height z_v. Thus, we have established that the difference L_2-L_1 is the number of vortices running from top to side. Next we show that a L_1 GV state is at the center. As one approaches the central axis (decreasing ρ), ψ_{L_2} vanishes before ψ_{L_1} because of its larger angular momentum barrier, assuming that $L_2>L_1$. Thus very close to the origin the two-component wave function reduces to $\Psi\sim C_{L_1}\psi_{L_1}\exp(iL_1)$, which means that the phase $\exp(iL_1\varphi)$ describes a top to bottom GV state provided that ψ_{L_1} vanishes at the axis of symmetry.

The notation adopted in this work is the same used in Ref. 32: (L_1,L_2) indicates a MV state whose order parameter is formed by ψ_{L_1} and ψ_{L_2}. The total vorticity is L_2 that splits into a L_1 GV state, piercing the rod from top to bottom, and L_2-L_1 top to side vortices. Notice that, according to this notation, a GV state can be expressed equivalently as L GV or as (L,L) MV because in this last case, there is no top to side vortices.

We find here that the rod displays two kinds of MV states, distinguishable by how they arise and disappear from the parent GV state. Consider a MV state obtained from a L_1 GV state by the increase in μ beyond some critical value. L_2-L_1 top to side vortices spring from the top surface and lead to a (L_1,L_2) MV state. We find in our numerical solutions that there are two different ways for this state to disappear at some higher critical μ. (i) The top to side vortices return to the top surface where they vanish and the original L_1 GV line is retrieved. (ii) The top to side vortices move to the bottom surface giving rise to a L_2 GV state, namely, to a total vorticity of $(L_2-L_1)+L_1$ along the axis.

The usefulness of the two-component approach is limited to rods with a small radius because in this case, curved vor-

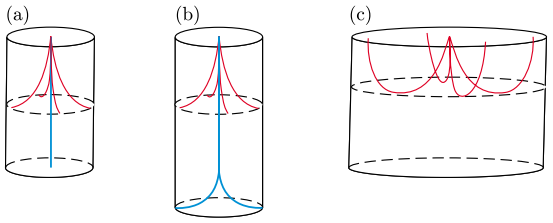

FIG. 2. (Color online) Three conceivable vortex patterns are shown here. In (a) the top to bottom (blue) line represents one giant vortex and the four top to side (red) lines represent single vortices. In (b) a further splitting of the giant vortex of (a) takes place yielding two single top to side vortices. In (c) top to top vortices arise because of the large radius. The only pattern that can be described by the present method is (a).

tices do not return to the top surface. Besides no second splitting of vortex lines inside the rod is possible, meaning that all top to side vortices exit at the same height. In this case, the two-component approach is able to describe top to side and top to bottom vortices entering the rod through its center. Figure 2 summarizes through a pictorial view the limits of applicability of the two-component approach. Figure 2(a) shows a (2, 6) MV state, assuming that at the center there is a 2 GV state. This situation is well described by a single two-component order parameter. Figure 2(b) presents a situation beyond the scope of the present work because the whole rod cannot be described by a single two-component order parameter, although different heights can be treated by distinct two-component order parameters. At the top the state is the same one of Fig. 2(a), namely, a (2,6) MV state, that becomes a 2 GV [or equally a (2,2) MV] below to finally turn into a (0,2) MV state. The case of Fig. 2(c), with a three-point intercept, is totally beyond the two-component order parameter since a z plane intercepts twice a vortex line, which added to a central vortex makes a total of three intercepts.

The correctness of the two-component method is confirmed by the simulated annealing method applied to the present problem[34] as both methods lead to the same vortex pattern. The onset of a second branch of vortices that splits below the first branch is never observed using this method for the radii considered here and for a wide range of heights. The simulated annealing method has been applied before to several other mesoscopic systems[19,31,33] and makes no assumptions about the number of angular components in the order parameter. We conclude that no further splitting of the vortices from the top takes place in the rod because of the weak magnetic field at the bottom and the curvature of the field which favors the exit of vortex lines at the lateral surface and not at the bottom surface. Another argument against a second splitting of the vortices from the top comes from Tables I–III. The data shown in these tables support the view that as the height increases, top to bottom vortices tend to disappear. For instance, the $R=2\xi$ rod only has for a top to bottom vortex the 1 GV state, and so, no splitting is possible for this rod regardless of its height. Similarly, the $R=3\xi$ and 4ξ rods have as the maximum sustainable top to bottom vorticity, beyond the 5ξ and 8ξ heights, respectively, the 1 GV state, which renders further splitting of these lines impossible beyond these heights.

Recently Aladyshkin *et al.*[35] have treated the vortex pattern of the rod in presence of a magnetic moment on its top added to a homogeneous magnetic field, both oriented along the central axis. His approach is limited to a one-component order parameter, fitted to obtain the upper critical field using the linearized theory. Since only vortex states with azimuthal symmetry were included there, top to side vortices are excluded, as they demand at least two components in the order parameter.

III. GINZBURG-LANDAU THEORY

The GL theory gives the Gibbs free energy of the superconductor near the critical temperature T_c by assuming its expansion in powers of a complex order parameter $\Psi(\vec{r})$ that gives the density of Cooper pairs, $|\Psi(\vec{r})|^2$. The Ginzburg-Landau approach to the mesoscopic superconductor has been discussed in many references, such as in Ref. 36. In this section, we treat the GL theory assuming that the order parameter is expressed as a linear expansion of solutions of the linear GL equation, limited to a maximum of two terms. Due to the mesoscopic size, the London penetration length is much larger than the dimensions of the rod and so the magnetic field inside and outside the rod are taken as equal. Hence the Gibbs free-energy difference between the superconducting and the normal states is

$$F_s - F_n = \int dV \left\{ \alpha(T)|\Psi|^2 + \frac{1}{2}\beta|\Psi|^4 + \frac{\hbar^2}{2m^*} \left| \times \left(\vec{\nabla} - i\frac{2\pi}{\Phi_0}\vec{A} \right)\Psi \right|^2 \right\} \tag{4}$$

with the phenomenological constants $\alpha(T) \equiv \alpha_0(T-T_c) < 0$, $\beta > 0$, m^* (the mass of one Cooper pair), and $\Phi_0 = hc/2e$, the fundamental unit of flux. The magnetic potential is $\vec{A} = \mu\rho/[\rho^2+(z-z_1)^2]^{3/2}\vec{e_\varphi}$ and the magnetic dot occupies the position $(0,0,z_1)$. Boundary conditions are imposed to the external surfaces of the rod. We express quantities in this theory in dimensionless units defined by the following reduced units: the coherence length $\xi(T)=[-\hbar^2/2m^*\alpha(T)]^{1/2}$ (lengths), $H_{c2}=\phi_0/2\pi\xi(T)^2$ (magnetic field), $H_{c2}\xi = \Phi_0/2\pi\xi(T)$ (vector potential), $\mu_0 = H_{c2}\xi(T)^3 = \Phi_0\xi(T)/2\pi$ (magnetic moment), $\Psi_0 = \sqrt{-\alpha(T)/\beta}$ (order parameter), and $F_0 = \alpha(T)^2/2\beta$ (free energy). In terms of these dimensionless units, the Gibbs free-energy difference becomes

$$F = 2\int dV \left\{ -|\Psi|^2 + \frac{1}{2}|\Psi|^4 + |(\vec{\nabla} - i\vec{A})\Psi|^2 \right\}. \tag{5}$$

The integration is restricted to the volume of the rod. The boundary condition in dimensionless units becomes

$$\vec{n}\cdot(\vec{\nabla} - i\vec{A})\Psi|_{boundary} = 0. \tag{6}$$

Following Ref. 25, we introduce the $\hat{L}$ linear operator, in terms of which the nonlinear GL equation becomes

$$\hat{L}\psi = -|\psi|^2\psi, \quad \hat{L} \equiv -(\vec{\nabla} - i\vec{A})^2 - 1. \tag{7}$$

Consequently, only the negative eigenvalues Λ of this $\hat{L}$ correspond to the superconducting state.

TABLE I. The sequence of ground states for the $R=2\xi$ set of rods is given here. The left column displays the height of the rods. The ground state (i) ranges between transition magnetic moments μ_α/μ_0 and μ_β/μ_0, as shown in the table.

z_0/ξ	μ_1/μ_0	1	μ_2/μ_0	2	μ_3/μ_0	3	μ_4/μ_0
2	0	0 GV	16.6	1 GV	32.9		
3	0	0 GV	38.2	1 GV	60.0		
4	0	0 GV	70.3	1 GV	100		
6	0	0 GV	100				
8	0	0 GV	14.0	(0,1) MV	17.0	0 GV	100
10	0	0 GV	11.0	(0,1) MV	22.0	0 GV	100

The following linear equation must be solved:

$$\hat{L}\psi_{L,n}(\rho,z)=\Lambda_{L,n}\psi_{L,n}(\rho,z), \tag{8}$$

where n enumerates the different states at a certain angular momentum quantum number L. Following Refs. 37 and 38, we restrict ourselves to $n=0$. This operator expressed in dimensionless units and in cylindrical coordinates becomes

$$\hat{L}=-\frac{1}{\rho}\frac{\partial}{\partial\rho}\left(\rho\frac{\partial\Psi}{\partial\rho}\right)-\frac{\partial^2\Psi}{\partial z^2}+\frac{1}{\rho^2}\left(L-\frac{\mu\rho}{[\rho^2+(z-z_1)^2]^{3/2}}\right)^2-1. \tag{9}$$

For the GV state described by Eq. (1), the coefficient C_L is a constant to be determined by imposing the condition of minimum free energy in Eq. (5). One obtains

$$C_L=\pm\sqrt{-\Lambda_L\frac{B_L}{A_L}} \tag{10}$$

and for the free energy,

$$F=-2\pi\Lambda_L^2\frac{B_L^2}{A_L}, \tag{11}$$

and the constants A_L e B_L are particular cases of Eqs. (14) and (15), discussed below. Inspection of the second derivative of the free energy shows that a negative eigenvalue Λ_L is the condition to render the state stable.

For the MV state of Eq. (2), it does not matter whether the coefficients C_{L_i} are real or complex because the choice does not affect the value of the free energy, and so, we can regard them as real according to Ref. 32. By minimizing the Gibbs free energy with respect to C_{L_1} and C_{L_2} using Eqs. (2) and (5), we obtain the following equilibrium states. (i) The normal state with $\Psi(\rho,\varphi,z)=0$ corresponds to $C_{L_1}=C_{L_2}=0$. (ii) The GV state with $C_{L_2}=0$ is $\Psi(\rho,\varphi,z)=C_{L_1}\psi_{L_1}e^{iL_1\varphi}$ with $C_{L_1}=(-\Lambda_{L_1}B_{L_1}/A_{L_1})^{1/2}$; the $C_{L_1}=0$ state is $\Psi(\rho,\varphi,z)=C_{L_2}\psi_{L_2}e^{iL_2\varphi}$ with $C_{L_2}=(-\Lambda_{L_2}B_{L_2}/A_{L_2})^{1/2}$. (iii) The MV state of Eq. (2) has the coefficients,

$$C_{L_1}=\pm\left(\frac{\Lambda_{L_1}A_{L_2}B_{L_1}-2\Lambda_{L_2}A_{L_1,L_2}B_{L_2}}{-A_{L_1}A_{L_2}+4A_{L_1,L_2}^2}\right)^{1/2},$$

$$C_{L_2}=\pm\left(\frac{\Lambda_{L_2}A_{L_1}B_{L_2}-2\Lambda_{L_1}A_{L_1,L_2}B_{L_1}}{-A_{L_1}A_{L_2}+4A_{L_1,L_2}^2}\right)^{1/2}. \tag{12}$$

The coefficients are determined by the following integrals:

$$A_{L_1,L_2}=\int_0^{z_0}dz\int_0^R\rho d\rho\psi_{L_1}^2(\rho,z)\psi_{L_2}^2(\rho,z), \tag{13}$$

$$A_{L_i}=\int_0^{z_0}dz\int_0^{R)}\rho d\rho\psi_{L_i}^4(\rho,z), \tag{14}$$

and

TABLE II. The sequence of ground states for the $R=3\xi$ set of rods is given here. The left column displays the height of the rods. The ground state (i) ranges between transition magnetic moments μ_α/μ_0 and μ_β/μ_0, as shown in the table.

z_0/ξ	μ_1/μ_0	1	μ_2/μ_0	2	μ_3/μ_0	3	μ_4/μ_0	4	μ_5/μ_0	5	μ_6/μ_0	6	μ_7/μ_0
2	0	0 GV	10.3	1 GV	19.8	2 GV	28.8	3 GV	38.6	4 GV	50.0		
3	0	0 GV	12.9	1 GV	27.8	2 GV	59.1	3 GV	72.0				
4	0	0 GV	15.3	1 GV	64.5	2 GV	98.5	3 GV	100				
5	0	0 GV	17.0	(0,2) MV	20.5	(0,3) MV	32.5	(0,4) MV	36.9	0 GV	44.9	1 GV	100
9	0	0 GV	10.8	(0,1) MV	11.6	(0,2) MV	30.4	(0,3) MV	42.0	0 GV	100		
10	0	0 GV	9.0	(0,1) MV	14.1	(0,2) MV	46.0	0 GV	100				
12	0	0 GV	7.9	(0,1) MV	16.7	(0,2) MV	100						
15	0	0 GV	6.8	(0,1) MV	20.0	(0,2) MV	100						

TABLE III. The sequence of ground states for the $R=4\xi$ set of rods is given here. The left column displays the height of the rods. The ground state (i) ranges between transition magnetic moments μ_α/μ_0 and μ_β/μ_0, as shown in the table. The states represented in bold face are those shown in Figs. 3 and 4.

z_0/ξ	μ_a/μ_0	i	μ_b/μ_0	$i+1$	μ_c/μ_0	$i+2$	μ_d/μ_0	$i+3$	μ_e/μ_0	$i+4$	μ_f/μ_0	$i+5$
2	0	0 GV	8.6	1 GV	16.7	2 GV	24.3	3 GV	31.9	4 GV	39.5	5 GV
	47.1	6 GV	54.8	7 GV	62.6	8 GV	70.8	9 GV	80.1	10 GV	87.0	
3	0	0 GV	10.5	1 GV	20.0	2 GV	29.0	3 GV	38.9	4 GV	64.2	5 GV
	82.7	6 GV	99.0	7 GV	100							
4	0	0 GV	11.7	1 GV	22.8	2 GV	38.0	**(2,6) MV**	48.2	**(2,7) MV**	58.7	**(3,8) MV**
	63.0	3 GV	82.3	4 GV	100							
6	0	0 GV	12.8	1 GV	21.0	**(0,3) MV**	30.3	**(0,4) MV**	39.4	**(1,5) MV**	45.5	**(1,6) MV**
	52.8	**(1,7) MV**	59.0	**(1,8) MV**	64.8	**(1,9) MV**	68.0	1 GV	87.4	2 GV	100	
8	0	0 GV	10.9	(0,2) MV	22.7	(0,3) MV	35.4	(0,4) MV	47.0	(0,5) MV	53.5	(0,4) MV
	68.7	1 GV	100									
10	0	0 GV	9.0	(0,2) MV	26.6	(0,3) MV	72.3	(0,4) MV	100			
14	0	0 GV	7.0	(0,1) MV	14.1	(0,2) MV	60.1	(0,3) MV	100			
20	0	0 GV	5.7	**(0,1) MV**	19.3	**(0,2) MV**	100					

$$B_{L_i} = \int_0^{z_0} dz \int_0^R \rho d\rho \psi_{L_i}^2(\rho,z). \tag{15}$$

The free energy of the GV state is

$$F_{L_i} = -2\pi\Lambda_{L_i}^2 \frac{B_{L_i}^2}{A_{L_i}}, \quad i=1,2 \tag{16}$$

and that of the MV state,

$$F_{L_1,L_2} = \frac{2\pi}{A_{L_1}A_{L_2} - 4A_{L_1,L_2}^2}(-\Lambda_{L_1}^2 A_{L_2} B_{L_1}^2 - \Lambda_{L_2}^2 A_{L_1} B_{L_2}^2 + 4\Lambda_{L_1}\Lambda_{L_2} A_{L_1,L_2} B_{L_1} B_{L_2}). \tag{17}$$

The stability of the two-component order parameter must be analyzed in terms of the Hessian matrix, as done in Ref. 32. The stability of the GV state, in case of $C_{L_1}=0$ and $C_{L_2}\neq 0$ is, a negative eigenvalue, $\Lambda_{L_2}<0$, and $\Lambda_{L_1}A_{L_2}B_{L_1} - 2\Lambda_{L_2}A_{L_1,L_2}B_{L_2} > 0$. There are three conditions to render the MV state stable, namely,

$$\Lambda_{L_1}A_{L_2}B_{L_1} - 2\Lambda_{L_2}A_{L_1,L_2}B_{L_2} > 0,$$

$$\Lambda_{L_2}A_{L_2}B_{L_1} - 2\Lambda_{L_2}A_{L_1,L_2}B_{L_2} > 0,$$

and

$$4A_{L_1,L_2} - A_{L_1}A_{L_2} > 0. \tag{18}$$

All results of this paper correspond to numerical solutions of Eq. (8) under the appropriate boundary condition of Eq. (6), applied to the external surfaces of the rod. We solve the linear GL equation for the rod through the finite-element method (COMSOL and MATLAB softwares) and then calculate the Gibbs free energy of the nonlinear theory. The stability of GV and MV states is checked during our numerical procedure. The one- and two-component order parameters of Eqs. (1) and (2) describe the GV and MV states, respectively.

IV. VORTEX PATTERNS

Based on the theory of the previous sections, we investigate here three sets of superconducting rods, with radii $R=2\xi$, 3ξ, and 4ξ, respectively, subject to the magnetic field of the magnetic dot put on its top. Each of the three sets contains selected heights, ranging from the shortest rod, $z_0=2\xi$, to the longest one, $z_0=5R$, and intermediate heights. The results are obtained within the magnetic moment range $\mu/\mu_0=0$ to 100. The magnetic-moment unit, previously defined as $\mu_0=\Phi_0/2\pi\xi$, corresponds to nearly a million oriented Bohr magnetons ($\xi/r_c\approx 10^6$, for a coherence length $\xi \approx 3.0$ nm. Notice that the Bohr magneton can also be expressed through a length, $\mu_B=\Phi_0 r_c/2\pi$, where r_c is the electron classical radius.[33] The magnetic dot must have size slightly larger than the coherence length. For instance, if spherical, it must have a radius $r_M=1.7\xi$. This is required in order to reach the saturation magnetization, $M=\mu_B/(4\pi a_0^3/3)=1.49$ T, defined here as being one Bohr magneton per atom, where $a_0\approx 0.05$ nm is the atomic radius. Nevertheless there is another adjustable parameter, the distance of the magnetic moment to the bottom of the rod, z_1. We choose to keep the magnetic moment at the fixed distance of 2ξ above the top of the rod, which means that $z_1 - z_0 = 2\xi$. Changing this distance or adjusting the intensity of the magnetic moment are not independent procedures. Experimentally they can be useful since the dot has finite dimensions and to achieve the truly nonhomogeneous magnetic field, fundamental in order to observe the predicted phenomena, the distance to the top surface becomes a key parameter. Notice the following invariance property under a scaling transformation by λ for the magnetic field $\boldsymbol{B}=[3(\boldsymbol{\mu}\cdot\hat{r})-\boldsymbol{\mu}]/r^3$: $\boldsymbol{B}(\mu,r,z_1/\lambda)=\boldsymbol{B}(\lambda^3\mu,\lambda r,z_1)$. Thus approaching the magnetic dot by $1/\lambda$ is equivalent to an increase in the magnetic moment by λ^3. The two situations yield fields with the same intensity at locations r and λr, respectively.

In this paper, we have obtained the ground states and their respective ranges of magnetic moments for the three sets of

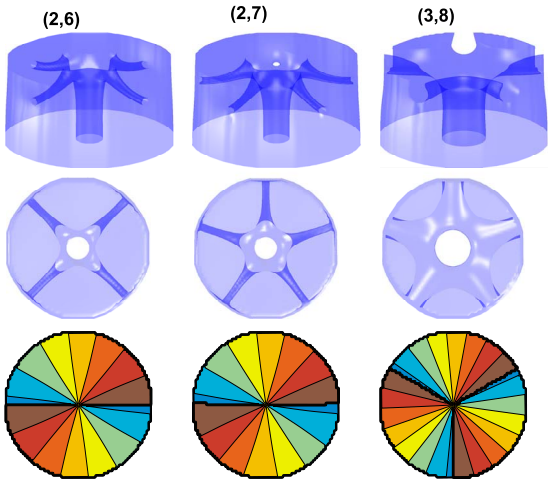

FIG. 3. (Color online) The topmost sequence of plots are isodensity three-dimensional (blue) plots corresponding to the (2,6), (2,7), and (3,8) states. The middle row shows the first two states from a top view of the rod while the last one from a bottom view. The lower plots are two-dimensional plots of the phase, taken at the bottom of the rod. The blue to red hue corresponds to a scale ranging from 0 to 2π and reveals angular momentum 2, 2, and 3 for these states (left to right). The three states are ground states of the $(R=4\xi, z_0=4\xi)$ rod, as shown (bold face) in Table III.

rods, with radii $R=2\xi$, 3ξ, and 4ξ, respectively. Their values are summarized in Tables I–III. The left column of these tables contains the respective height considered, ranging from the shortest rod, $z_0=2\xi$, to the longest one, $z_0=5R$. We summarize the notation previously developed for the (L_1, L_2) MV, assuming $L_2 \geq L_1$, as follows: L_1 is the vorticity of the top to bottom giant vortex, there are L_2-L_1 single vorticity top to side vortices and the total vorticity is L_2.

Figures 3 and 4 provide some examples of the MV states obtained here. The semitransparent figures are three-dimensional surface plots, that is, isodensity plots with two kinds of surfaces. The inner ones are the vortices inside the rod and the outer one is very near to the rod's external surface. They are obtained by fixing $|\psi|^2$ to a constant value, chosen near to zero so to help visualize the center of the vortices, where the order parameter must vanish. The different colors used in the three-dimensional surface plots of Fig. 4 mean rods with distinct geometrical parameters. Figure 3 also contains two-dimensional phase plots, shown below the corresponding three-dimensional surface plots. They are taken at the bottom surface of the rod and show that indeed the (2,6) MV and (2,7) MV have the same vorticity, equal to a 2 GV state whereas the (3,8) MV has vorticity of a 3 GV state. This conclusion can be directly inferred by the number of hues observed in the phase plots, as discussed elsewhere.[36,39]

The simplest set of rods has $R=2\xi$ and shows a reentrant behavior. Six distinct heights ($z_0=2\xi$, 3ξ, 4ξ, 6ξ, 8ξ, and 10ξ) are analyzed here. The ground states and their respective ranges are summarized in Table I. The free energy versus magnetic-moment plots are shown in Fig. 5. The shortest rod, $z_0=2\xi$, only has GV states. The 1 GV state is a ground state for the $z_0=2\xi$, 3ξ, and 4ξ but not for the last two longest rods considered, namely, 8ξ and 10ξ, where it is just an excited vortex state. The 2 GV state never becomes a ground state, only exists as an excited one. For the 3ξ, and longer ones, it is not even present. According to our previous discussion, long rods cannot sustain GV states. Notice the increase in the upper critical field as the rods become longer. For the $z_0=4\xi$ rod, it falls beyond the magnetic-moment range studied here. Notice that for the 6ξ rod, no GV states are possible at all, and so this rod is empty of vortex states. The 0 GV and 1 GV lines do not cross each other within the studied range, and so, the 1 GV state is not possible there. The last two longest rods show a turn around in this trend set by the 6ξ rod. There we find the onset of the (0,1) MV state, a single vortex line piercing the rod top to side. The (0,1) MV state is of type (i) since its onset and disappearance is from the 0 GV line. Thus it exists within a finite magnetic-moment range and once the maximum moment is reached this vortex is expelled from where it came from, the top surface. Since the 0GV state is retrieved, a reentrant behavior is observed here. This (0,1) MV state begins at some critical height z_0 and its window grows by increasing the rod's height up to some saturation window. Among the studied set of rods, this has the simplest behavior since it does not tolerate more than one GV and also no more than one MV state. Notice that reentrant behavior is very much connected with the minimal geometrical condition for the onset of a single

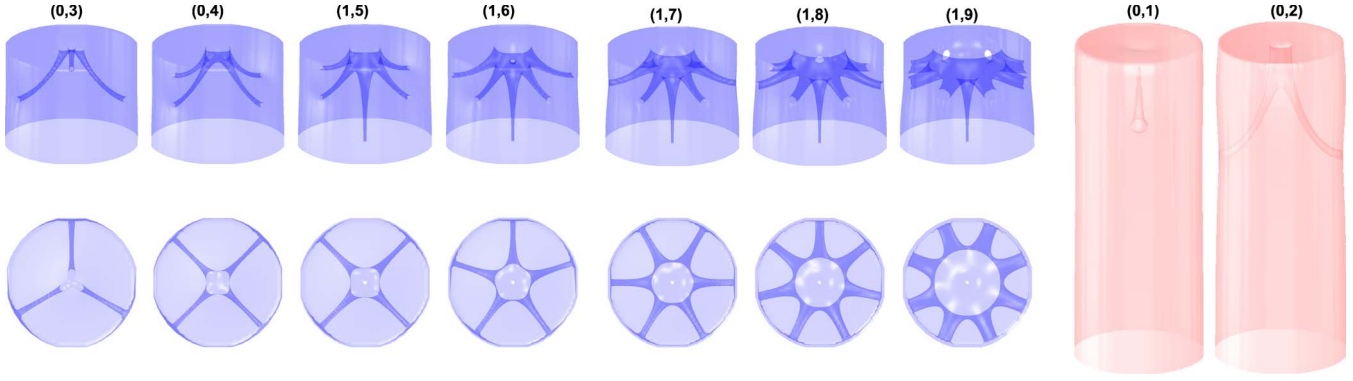

FIG. 4. (Color online) Two sequences of isodensity three-dimensional plots are shown for the $(R=4\xi, z_0=6\xi)$ (magenta) and $(R=4\xi, z_0=20\xi)$ (red) rods, respectively. They correspond to the sets [(0,3),(0,4),(1,5),(1,6),(1,7),(1,8),(1,9)] and [(0,1),(0,2)], respectively, as seen in Table III. These are ground states of the rod, as shown (bold face) in Table III.

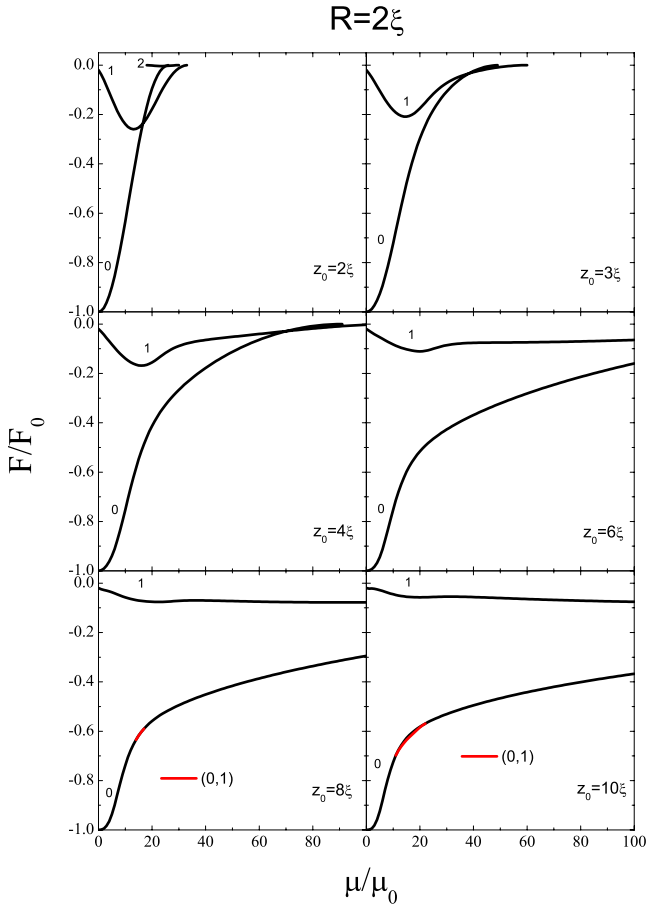

FIG. 5. (Color online) The free energy versus magnetic moment is shown for the set of cylindrical rods with radius $R=2\xi$. Six distinct heights are considered, $z_0=2\xi$, 3ξ, 4ξ, 6ξ, 8ξ, and 10ξ. (Black) lines are giant-vortex states labeled by their angular momentum L. The only possible multivortex state is the (red) line (0,1) MV. All the existing states within the studied range are shown here.

vortex. As shown here, the reentrant behavior is a consequence of competing geometrical and physical parameters. Mesoscopic superconductors in the presence of a constant applied external field do not display reentrant behavior, although they do have minimal geometrical requirements for the entrance of a single vortex. For a superconducting disk, the entrance of a vortex depends on its radius, R.[39] If comparable to the coherence length, ξ, only the Meissner state is possible, but for $\xi<R<2\xi$, giant-vortex states are allowed while for $R>2\xi$, multivortex states become possible.

The set of rods with $R=3\xi$ has its ground states and their respective ranges summarized in Table II. Their free energy versus magnetic-moment plots are shown in Fig. 6. Eight heights are considered ($z_0=2\xi$, 3ξ, 4ξ, 5ξ, 9ξ, 10ξ, 12ξ, and 15ξ). This set is richer than the previous one because more vortices can fit inside the rod. The GV states range from 0 GV to 5 GV for the shortest one, $z_0=2\xi$, although the 5 GV is only an excited state. The normal state is reached by the 4 GV state at $\mu/\mu_0=50.0$. Increasing the height shifts the upper critical field upward. For the $z_0=3\xi$ rod, the normal state is reached at a higher moment, $\mu/\mu_0=72.0$. The 5 GV state no longer exists and the 4 GV becomes just an excited state. For the $z_0=4\xi$ rod, we see the onset of the (0,3) MV and (0,4) MV states, though just as excited states since the 1 GV is the ground state within the range of their existence. For the next case, the $z_0=5\xi$ rod, these MV states become ground states in sequence: (0,2) MV, (0,3) MV, and (0,4) MV, as summarized in Table III. They all arise and disappear from the 0 GV line, and the last one is replaced by the 1 GV state as the ground state. For the $z_0=9\xi$ rod, we observe the onset of the (0,1) MV state within a very small range and just as an excited state. However, it becomes a ground state for the $z_0=10\xi$ rod. For the last four rods studied ($z_0=9\xi$, 10ξ, 12ξ, and 15ξ) the 0 GV, 1 GV, and 2 GV lines do not cross each other, and so, only the 0 GV qualifies for a ground state. We notice that in this regime of nonintersecting GV lines, all MV lines start and end from a single GV line [type (i)]. Consequently MV states which are ground states arise and end from the 0 GV line, characterizing a reentrant behavior, like the one found in the previous set of rods. This reentrant behavior is seen for the $z_0=10\xi$ but not for the two longest rods. There it is impossible to expel the (0,2) MV state. We have checked that this is true beyond the magnetic-moment range studied here, namely, up to $\mu/\mu_0=1000$. For the $z_0=12\xi$ and the 15ξ, only (0,1) MV and (0,2) MV states are MV ground states.

For the $R=4\xi$ rods, we consider eight possible heights ($z_0=2\xi$, 3ξ, 4ξ, 6ξ, 8ξ, 10ξ, 14ξ, and 20ξ). The shortest rod ($z_0=2\xi$) has 12 GV states ($L=0-11$) but the highest one in angular momentum, the 11 GV state, is only an excited state. The remaining states, from 0 GV to 10 GV, become ground states within specific ranges, as shown in Table III. Notice that the superconducting state is destroyed at $\mu/\mu_0=87.0$ thus below the maximum studied value of $\mu_{\max}/\mu_0=100$. There are no MV states in this case. For the $z_0=3\xi$ rod, the number of GV states drops to 8 states ($L=0-7$) and the upper critical field falls beyond the studied range. This rod has MV states of the second kind, (ii), previously introduced, as they are bridges connecting different GV states. The following MV states are observed for this rod:(0,4), (0,5), (0,6), (0,7), (1,5), (1,6), (1,7), (1,8), (2,6), (2,7), (2,8), (2,9), and (3,8). For the $z_0=4\xi$ rod, there are 8 GV states ($L=0-7$) but only the 0 GV, 1 GV, 2 GV, 3 GV, and 4 GV are ground states. The following MV states are observed: $(0,k_0)$, $k_0=3-9$, $(1,k_1)$, $k_1=4-9$ $(2,k_2)$, $k_2=5-9$, $(3,k_3)$ $k_3=7-9$. Table III lists those that are ground states. There are also 8 GV states ($L=0-7$) for the $z_0=6\xi$ rod and 2 GV, 3 GV, 4 GV, and 5 GV lines form a set of nonintersecting lines, thus among them only the lowest one, 2 GV, qualifies for a ground state. Indeed only 0 GV, 1 GV, and 2 GV become ground states. The following MV states are observed for this rod:$(0,k_0)$, $k_0=3-9$, $(1,k_1)$, $k_1=4-9$, $(2,k_2)$, $k_2=7-9$, $(3,k_3)$ $k_3=7-9$. Table III only lists those that are ground states. For the $z_0=8\xi$ rod, there are 8 GV states ($L=0-7$). Only the 0–5 GV lines reach the maximum studied value of $\mu_{\max}/\mu_0=100$, others disappear before, at different critical magnetic moments. The lines 2–7 GV are nonintersecting, and so, only 2 GV among them qualifies as a ground state. Nevertheless it never becomes one and only 0 GV and 1 GV are, as listed in Table III. The following MV states are observed for this rod: $(0,k_0)$, $k_0=2-9$, $(1,k_1)$, $k_1=3-9$, $(2,k_2)$, $k_2=5-9$, and (3,8), and those that become ground states are

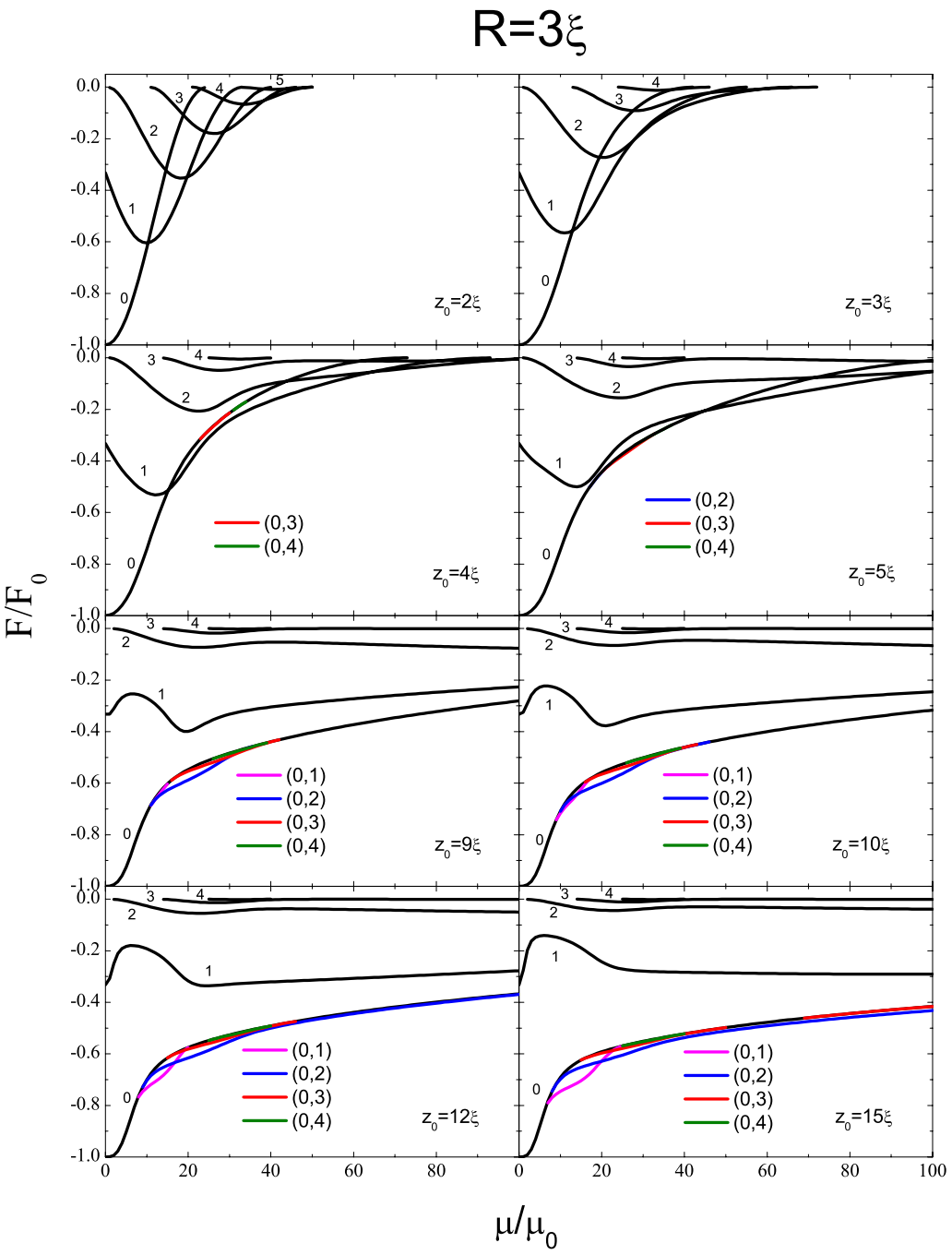

FIG. 6. (Color online) The free energy versus magnetic moment is shown for the set of cylindrical rods with radius $R=3\xi$. Six distinct heights are considered, $z_0=2\xi$, 3ξ, 4ξ, 5ξ, 9ξ, 10ξ, 12ξ, and 15ξ. (Black) lines are giant-vortex states labeled by their angular momentum L. Multivortex states are (colored) lines labeled by (L_1,L_2). All the existing states within the studied range are shown here.

listed in Table III. The $z_0=10\xi$ rod displays the same GV state behavior of the previous case. The following MV states are observed for this rod: $(0,k_0)$, $k_0=1-9$, $(1,k_1)$, $k_1=3-9$, $(2,k_2)$, $k_2=5-9$, and (3,8) and Table III only lists those that become ground states, namely, (0,2) MV, (0,3) MV, and (0,4) MV. For the $z_0=14\xi$ rod, only the 0–5 GV lines reach the maximum magnetic moment, like found for the two previous rods. All GV lines are nonintersecting ones, and so, only the 0 GV line can be a ground state. Of the observed MV states, $(0,k_0)$, $k_0=1-9$, $(1,k_1)$, $k_1=3-9$, $(2,k_2)$, $k_2=5-9$, and (3,8), only (0,1) MV, (0,2) MV, and (0,3) MV are ground states, as listed in Table III. The $z_0=20\xi$ rod has the same features of the previous case, however only (0,1) MV and (0,2) MV are ground states according to Table III. These states do not return to the 0 GV line even beyond the magnetic-moment range studied, at least up to $\mu/\mu_0=1000$.

Figure 7 shows the behavior of the first 6 GV lines ($L=0-5$) and MV states up to the (4,5) MV state for the $R=4\xi$ rod. Thus this figure does not display all the existing states for the studied rods ($z_0=2\xi$, 3ξ, 4ξ, 6ξ, 8ξ, 10ξ, 14ξ, and 20ξ). We choose not to show all states in Fig. 7 to help the reader visualize the lowest angular momentum lines. This

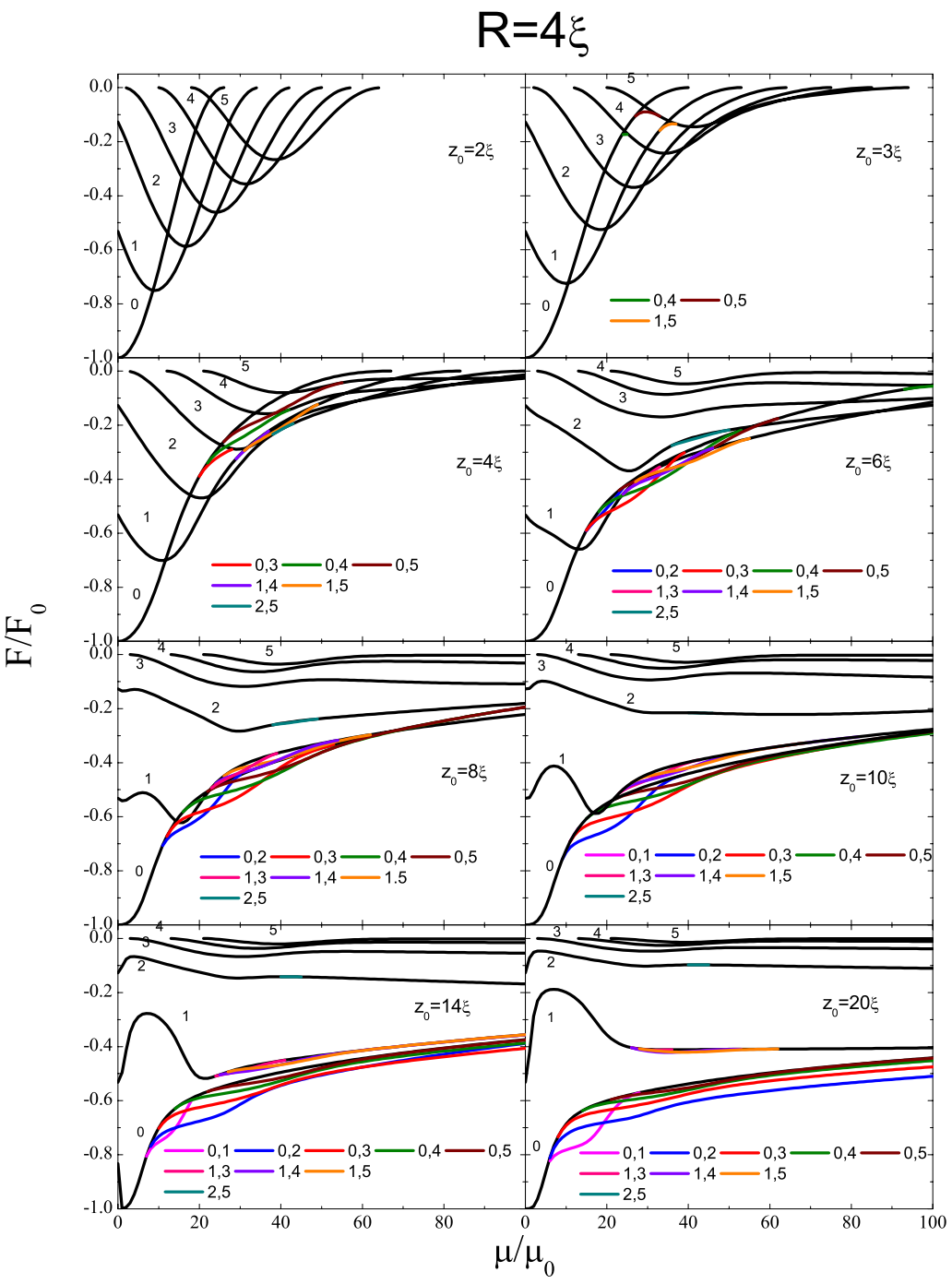

FIG. 7. (Color online) The free energy versus magnetic moment is shown for the set of cylindrical rods with radius $R=4\xi$. Six distinct heights are considered, $z_0=2\xi$, 3ξ, 4ξ, 6ξ, 8ξ, 10ξ, 14ξ, and 20ξ. (Black) lines are giant-vortex states labeled by their angular momentum L. Multivortex states are (colored) lines labeled by (L_1,L_2). Only states up to $L=5$ and $(L_1=4,L_2=5)$ are shown here.

is the most important aspect as the ground state of the rod in the long limit falls within these lines. For this reason, we follow the evolution of these first lines, as a function of the rod's height. The $R=4\xi$ family, besides being more complex than previous ones, also present novel features not found in the previous two sets. Notice that Fig. 7 displays for the shortest rod, $z_0=2\xi$, $\mu/\mu_0=64$ as the maximum moment reached by the 5 GV line, which is not the upper critical field. The $z_0=3\xi$ rod displays MV states of the second kind, (ii), previously discussed. They are not ground states and each one interconnect two distinct GV lines. Figure 7 shows the (0,4) MV line, which arises from the 0 GV line and ends in the 4 GV line. Similarly the (0,5) MV and the (1,5) MV lines bridge the 0 GV and the 1 GV lines, respectively, to the 5 GV line. Notice the absence of the (0,1) MV, (0,2) MV, and (0,3) MV states. The next case, $z_0=4\xi$, has MV of the two kinds, (i) and (ii). Figure 7 shows that the (0,3) MV, (0,4) MV, and (0,5) MV are type (ii) because they interconnect the 0 GV line to the 3 GV, 4 GV, and 5 GV lines, respectively. The (1,4) MV, (1,5) MV, and (2.5) MV are of type (i),

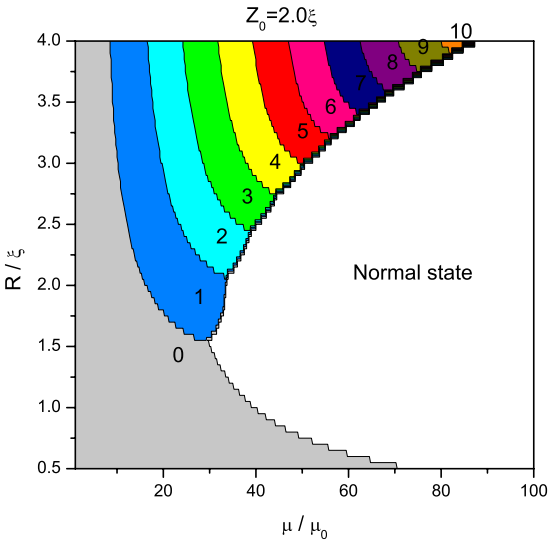

FIG. 8. (Color online) This plot shows the ground state of superconducting rods with height $z_0=2\xi$ according to the radius R and the strength μ of the magnetic dipole placed on the top of the rod. The ground state is only made of giant vortices that pierce the rod top to bottom.

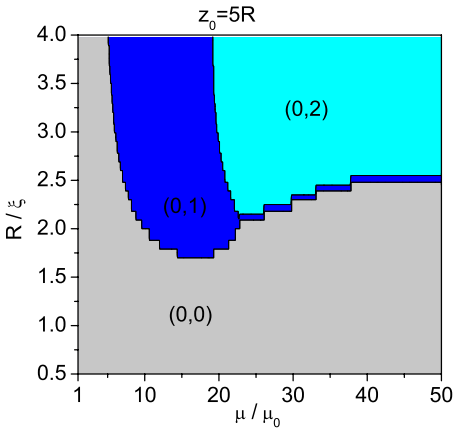

FIG. 9. (Color online) This plot shows the ground state of superconducting rods with height $z_0=5R$ according to the radius R and the strength μ of the magnetic dipole place on the top of the rod. The ground state is only made of multi vortices that pierce the rod top to side.

namely, they are not bridge states. The beginning and the end of these lines are in one single GV line. The (1,4) MV and (1,5) MV states belong to the 1 GV line, as the (2,5) MV belongs to the 2 GV line. According to Fig. 7, the (2,5) MV state is the lowest in energy but this is not so because there are lines not displayed there. Figure 7 suggests the sequence of ground states (0 GV, 1 GV, 2 GV, (2,5) MV, 2 GV, 3 GV, and 4 GV) which does not match the true ground-state sequence of Table III (0 GV, 1 GV, 2 GV,(2,6) MV,(2,7) MV, (3,8) MV,3 GV, and 4 GV). This is because not all lines are shown in Fig. 7, as previously discussed. The $z_0=6\xi$ rod is a very rich case, as it is intermediate between the short and the long limits, which according to Table III form the following sequence of ground states: 0 GV, 1 GV, (0,3) MV, (0,4) MV, (1,5) MV, (1,6) MV, (1,7) MV, (1,8) MV, (1,9) MV, 1 GV, and 2 GV). Notice the sequence given by Fig. 7: 0 GV, 1 GV, (0,3) MV, (0,4) MV, (1,5) MV, 1 GV, and 2 GV. The (0,3) MV state is the first MV ground state, and it takes over the 1 GV state as the ground state. For the $z_0=8\xi$ rod and longer ones, the ground states, as read from Fig. 7, are the true ones since they coincide with those of Table III. The $z_0=8\xi$ rod shows the curious feature that the 1 GV intersects the 0 GV three times ($\mu/\mu_0=24.3$, 22.5, and 66.3) and for $\mu/\mu_0=68.7$ overcomes the (0,4) MV line to become the ground state. For the $z_0=10\xi$ rod and longer ones, the $(0,L)$ MV lines emerging from the 0GV are the only ground states, but their return to the 0 GV line is not observed within the studied range. The (0,1) MV line is first seen in the $z_0=10\xi$ rod, within a very small range, ($\mu/\mu_0=11.0-13.0$) but only as an excited state. For the $z_0=14\xi$ rod, it becomes a ground state and for the longest one, $z_0=20\xi$, stabilizes within the range ($\mu/\mu_0=5.7-19.3$) as shown in Table III. Thus the major conclusion from Fig. 7 is that the (0,2) MV state is a very stable ground state for long rods which dominates most of the range with the exception of a small part at lower magnetic moment where the (0,1) MV state prevails.

The phase diagrams for the short and long rods best summarize our results. To obtain them, we determine the angular momentum of the ground state for each pair of values, (μ,R), in these two extreme cases. The plot R versus μ reveals for the short limit, taken as $z_0=2\xi$, that only top to bottom vortices are ground states, as seen in Fig. 8. In the opposite limit, we fix the height to be $z_0=5R$, where only top to side vortices qualify as ground states. Hence the height varies continuously with the radius in this diagram, ranging from $z_0=2.5\xi$ for $R=0.5\xi$ to $z_0=20.0\xi$ for $R=4.0\xi$. Figure 9 shows genuine MV states as there is no top to bottom vortices there, just top to side. The long-limit phase diagram shows reentrant behavior, as previously discussed that corresponds to the entrance and exit of a top to side vortex. The long rod of Fig. 9 never reaches the upper critical field but the short rod of Fig. 8 does it, as superconductivity is destroyed by a sufficiently strong μ. For instance, the linear increase in μ for a $R=2.0\xi$ short rod takes it from the 0 GV state to the 1 GV and next to the normal state, as seen in Figs. 5 and 8. We remark the presence of a triple state point in both diagrams. Figure 8 shows that 0 GV, 1 GV, and the normal state meet approximately at $(\mu/\mu_0\approx 30, R/\xi\approx 1.5)$. Figure 9 shows that (0,0) MV, (0,1) MV, and (0,2) MV meet approximately at $(\mu/\mu_0\approx 24, R/\xi\approx 2.2)$ and corresponds to the entrance and exit of a top to bottom vortex.

V. CONCLUSION

We have obtained here the vortex patterns of a mesoscopic rod with a magnetic moment put on its top. The moment is aligned with the rod's central axis. We find that vortex patterns change significantly according to the rod's height and radius and all this is described by the Ginzburg Landau theory. The order parameter has only two angular

components, which is sufficient to describe a vortex pattern made of a central vortex and of a single shell of surrounding vortices, and so, curved vortices, which exit the lateral surface, can be described within the present treatment. This is possible as long as the radius of the rod is small enough to forbid the return of the vortex lines to the top surface. No second splitting of the vortices inside the rod is considered here. Thus the vortex patterns are made of top to bottom and top to side vortices, well described here by giant and multivortex states, which dominate the short and long rods, respectively. We find truly reentrant behavior for long rods, an interesting feature that qualifies the superconducting rod with a magnetic moment on top for logical applications in electronic devices.

ACKNOWLEDGMENTS

The three authors acknowledge CNPq and the bilateral program between Brazil and Flanders for financial support. They also make the following acknowledgments for financial support: A.R. de C. Romaguera to FACEPE, M.M. Doria to FAPERJ, and F.M. Peeters to the Flemish Science Foundation (FWO-Vl), the Belgian Science Policy (IUAP), and the ESF-AQDJJ network.

*mmd@if.ufrj.br

[1] M. Velez, J. I. Martin, J. E. Villegas, A. Hoffmann, E. M. Gonzalez, J. L. Vicent, and I. K. Schuller, J. Magn. Magn. Mater. **320**, 2547 (2008).
[2] A. Y. Aladyshkin, A. V. Silhanek, W. Gillijns, and V. V. Moshchalkov, Supercond. Sci. Technol. **22**, 053001 (2009).
[3] H. Bluhm, S. E. Sebastian, J. W. Guikema, I. R. Fisher, and K. A. Moler, Phys. Rev. B **73**, 014514 (2006).
[4] H. Sakai, N. Osawa, K. Yoshimura, M. Fang, and K. Kosuge, Phys. Rev. B **67**, 184409 (2003).
[5] J. D. Jorgensen, O. Chmaissem, H. Shaked, S. Short, P. W. Klamut, B. Dabrowski, and J. L. Tallon, Phys. Rev. B **63**, 054440 (2001).
[6] C. Bernhard, J. L. Tallon, E. Brücher, and R. K. Kremer, Phys. Rev. B **61**, R14960 (2000).
[7] J. E. McCrone, J. L. Tallon, J. R. Cooper, A. C. MacLaughlin, J. P. Attfield, and C. Bernhard, Phys. Rev. B **68**, 064514 (2003).
[8] T. Nachtrab, D. Koelle, R. Kleiner, C. Bernhard, and C. T. Lin, Phys. Rev. Lett. **92**, 117001 (2004).
[9] G. Carneiro, Physica C **432**, 206 (2005).
[10] C. C. de Souza Silva, A. V. Silhanek, J. Van de Vondel, W. Gillijns, V. Metlushko, B. Ilic, and V. V. Moshchalkov, Phys. Rev. Lett. **98**, 117005 (2007).
[11] S.-L. Cheng and H. A. Fertig, Phys. Rev. B **60**, 13107 (1999).
[12] D. J. Priour and H. A. Fertig, Phys. Rev. Lett. **93**, 057003 (2004).
[13] M. V. Milošević and F. M. Peeters, Phys. Rev. Lett. **94**, 227001 (2005).
[14] M. V. Milošević, G. R. Berdiyorov, and F. M. Peeters, Phys. Rev. Lett. **95**, 147004 (2005).
[15] M. J. V. Bael, L. V. Look, M. Lange, K. Temst, G. Guntherodt, V. V. Moshchalkov, and Y. Bruynseraede, Physica C **341-348**, 965 (2000).
[16] M. J. Van Bael, L. Van Look, M. Lange, J. Bekaert, S. J. Bending, A. N. Grigorenko, K. Temst, V. V. Moshchalkov, and Y. Bruynseraede, Physica C **369**, 97 (2002).
[17] W. Gillijns, A. Y. Aladyshkin, M. Lange, M. J. Van Bael, and V. V. Moshchalkov, Phys. Rev. Lett. **95**, 227003 (2005).
[18] J. E. Villegas, C.-P. Li, and I. K. Schuller, Phys. Rev. Lett. **99**, 227001 (2007).
[19] A. R. de C. Romaguera, M. M. Doria, and F. M. Peeters, Phys. Rev. B **75**, 184525 (2007).
[20] M. V. Milošević, G. R. Berdiyorov, and F. M. Peeters, Appl. Phys. Lett. **91**, 212501 (2007).
[21] A. K. Geim, I. V. Grigorieva, S. V. Dubonos, J. G. S. Lok, J. C. Maan, A. E. Filippov, and F. M. Peeters, Nature (London) **390**, 259 (1997).
[22] A. K. Geim, S. V. Dubonos, J. G. S. Lok, M. Henini, and J. C. Maan, Nature (London) **396**, 144 (1998).
[23] A. K. Geim, S. V. Dubonos, J. J. Palacios, I. V. Grigorieva, M. Henini, and J. J. Schermer, Phys. Rev. Lett. **85**, 1528 (2000).
[24] P. S. Deo, V. A. Schweigert, F. M. Peeters, and A. K. Geim, Phys. Rev. Lett. **79**, 4653 (1997).
[25] V. A. Schweigert, F. M. Peeters, and P. S. Deo, Phys. Rev. Lett. **81**, 2783 (1998).
[26] I. V. Grigorieva, W. Escoffier, V. R. Misko, B. J. Baelus, F. M. Peeters, L. Y. Vinnikov, and S. V. Dubonos, Phys. Rev. Lett. **99**, 147003 (2007).
[27] M. F. Andersen, C. Ryu, P. Clade, V. Natarajan, A. Vaziri, K. Helmerson, and W. D. Phillips, Phys. Rev. Lett. **97**, 170406 (2006).
[28] A. Kanda, B. J. Baelus, F. M. Peeters, K. Kadowaki, and Y. Ootuka, Phys. Rev. Lett. **93**, 257002 (2004).
[29] M. M. Doria, A. R. de C. Romaguera, and F. M. Peeters, Phys. Rev. B **75**, 064505 (2007).
[30] B. J. Baelus, D. Sun, and F. M. Peeters, Phys. Rev. B **75**, 174523 (2007).
[31] A. R. de C. Romaguera, M. M. Doria, and F. M. Peeters, Phys. Rev. B **76**, 020505(R) (2007).
[32] Y. Chen, M. M. Doria, and F. M. Peeters, Phys. Rev. B **77**, 054511 (2008).
[33] M. M. Doria, A. R. de C. Romaguera, M. V. Milosevic, and F. M. Peeters, EPL **79**, 47006 (2007).
[34] A. R. de C. Romaguera, M. M. Doria, and F. Peeters, Physica C, doi:10.1016/j.physc.2010.02.069 (2010).
[35] A. Y. Aladyshkin, D. A. Ryzhov, A. V. Samokhvalov, D. A. Savinov, A. S. Mel'nikov, and V. V. Moshchalkov, Phys. Rev. B **75**, 184519 (2007).
[36] B. J. Baelus, F. M. Peeters, and V. A. Schweigert, Phys. Rev. B **61**, 9734 (2000).
[37] S. V. Yampolskii and F. M. Peeters, Phys. Rev. B **62**, 9663 (2000).
[38] V. A. Schweigert and F. M. Peeters, Phys. Rev. Lett. **83**, 2409 (1999).
[39] B. J. Baelus, F. M. Peeters, and V. A. Schweigert, Phys. Rev. B **63**, 144517 (2001).